Acceleration- and deceleration-phase nonlinear Rayleigh-Taylor growth at spherical interfaces

Daniel S. Clark* and Max Tabak
Lawrence Livermore National Laboratory, University of California, Livermore, California 94550, USA
(Received 22 April 2005; published 4 November 2005)

The Layzer model for the nonlinear evolution of bubbles in the Rayleigh-Taylor instability has recently been generalized to the case of spherically imploding interfaces [D. S. Clark and M. Tabak, Phys. Rev. E **71**, 055302(R) (2005)]. The spherical case is more relevant to, e.g., inertial confinement fusion or various astrophysical phenomena when the convergence is strong or the perturbation wavelength is comparable to the interface curvature. Here, the model is further extended to the case of bubble growth during the deceleration (stagnation) phase of a spherical implosion and to the growth of spikes during both the acceleration and deceleration phases. Differences in the nonlinear growth rates for both bubbles and spikes are found when compared with planar results. The model predictions are verified by comparison with numerical hydrodynamics simulations.

DOI: 10.1103/PhysRevE.72.056308 PACS number(s): 47.20.Ky, 47.40.−x, 52.57.Fg

I. INTRODUCTION

The Rayleigh-Taylor (RT) instability [1,2] results from the acceleration of a dense fluid by a less dense fluid. The resulting distortion of the fluid interface has been extensively studied in the context of inertial confinement fusion (ICF) [3] as well as various astrophysical applications [4–9]. During the linear phase of RT growth, perturbation amplitudes exponentiate in time but retain their phase relative to the initial conditions. Once the perturbation amplitude reaches some fraction of its wavelength [generally accepted as $O(\frac{1}{10})$], however, the unstable modes begin to couple nonlinearly, resulting in the formation of characteristic bubble and spike structures. At planar interfaces subject to a constant acceleration, these bubbles of low-density fluid rise into the dense fluid with a constant velocity while the spikes of dense fluid fall with constant acceleration. The late phase of growth is often characterized by highly turbulent mixing due to the formation of secondary Kelvin-Helmholtz (KH) instabilities. References [10] and [11] contain excellent reviews of the extensive literature on RT instabilities.

Since, in very many physical situations, RT instabilities develop on a spherical interface undergoing either implosion or explosion, the effects of spherical convergence on RT growth were introduced early on by Bell [12] and Plesset [13]. These analyses considered both compressible and incompressible fluids but addressed only the linear regime of RT growth. Simultaneously, building on the earlier work of Davies and Taylor [14], Layzer developed what is now the classic model for describing the early nonlinear phase of RT bubble growth at planar interfaces [15]. The central result of this work was the well-known bubble rise velocity $u \simeq \sqrt{gr_0/k_0}$. Here, g is the acceleration of the interface or an effective gravitational acceleration, r_0 is the bubble radius or perturbation wavelength, and k_0 is the first root of the Bessel function J_1. This result is restricted to irrotational, incompressible flow and assumes an Atwood number of $\mathcal{A}=1$, but nevertheless comports very well with both experiment [16] and numerical simulation [17].

Subsequently, Layzer's results were independently derived and placed on a more rigorous foundation by Kull [18]. As further developments, Hecht *et al.* [19] successfully applied the Layzer-type approach to the case of Richtmyer-Meshkov instabilities [20,21], while Zhang [22] showed that such models can be used to describe spike growth in addition to bubbles. These results are all strictly valid only for planar interfaces, and the important case of nonlinear growth at spherical interfaces remains to be adequately addressed. Growth at cylindrically imploding interfaces was considered by Yedvab *et al.* [23], though this analysis suffers from an unphysical (i.e., divergent) representation of the fluid velocity field near the cylindrical axis. Some early progress on growth at spherical interfaces was made by the numerical work of Henshaw *et al.* [24], Sakagami and Nishihara [25], and Town and Bell [26]. A satisfactory analytical foundation, however, analogous to the Bell-Plesset results for the linear regime or the Layzer model for the planar case, remains to be found.

Developing an analog of the Layzer model which correctly incorporates the effects of spherical convergence would be valuable on many accounts. Foremost, a theoretical analysis of RT growth during implosions is of considerable importance to upcoming ICF ignition experiments. The design and analysis of such experiments have heretofore relied exclusively on numerical simulation results or scaling laws based on planar theory. Previous numerical investigations have suggested that stronger nonlinear growth might occur in spherical systems than might be expected from their planar analogues. However, these results are without the theoretical foundation afforded the planar case by the Layzer model.

Note that, unique to imploding interfaces, RT growth can occur in two distinct phases: an acceleration phase, when the shell is being brought up to its peak inward implosion velocity and the outer surface is RT unstable, and a deceleration phase, when the shell stagnates at its peak compression and now the inner surface of the shell is unstable with respect to the high-pressure, low-density enclosed gas. Furthermore, in the ICF context, both RT bubbles and spikes are potentially

*Electronic address: clark90@llnl.gov

threatening to the goal of ignition: the growth of bubbles causes a thinning of the shell and may ultimately lead to breakup and consequent loss of compression. Alternately, during the deceleration phase, spikes of cold fuel can jet into the central hot spot of the fusion fuel and so quench ignition. Each of these aspects of convergent RT growth would benefit from a fuller investigation.

More generally, analytical solutions, such as Layzer's, complement numerical work in elucidating the scaling properties of a phenomenon over a wide range of physical parameters as well as affording valuable test problems to validate hydrodynamics codes. Nonlinear RT growth in a converging system presents a particularly relevant as well as rigorous test problem for ICF design codes. The spherical situation is especially pressing, in that codes can generally be benchmarked against experimental results when analytical benchmarks are absent. In the converging case, however, the measurement of nonlinear RT amplitudes is diagnostically quite challenging and at best indirect. Though some attempts have been made to study nonlinear growth at spherical interfaces experimentally [27], a direct, rigorous benchmarking remains elusive. Finally, a more complete understanding of the nonlinear phase of converging RT growth would generally be valuable in the development of inertial fusion energy. Capsules designed for energy production, and hence high gain, can be expected to "push the limits" of hydrodynamic instabilities. A precise understanding of the tolerable boundaries of instability growth, likely appearing during the weakly nonlinear phase, would then be highly useful in target design.

Here, a Layzer-type RT model is combined with the self-similar implosion models of the type initially studied by Kidder [28] to develop a RT model for spherically imploding interfaces. Only the intermediate stage of growth—i.e., once coherent bubble and spike structures have formed but before the onset of turbulent mixing—is considered. The model fully accounts for compressibility of the imploding fluid. Given their equal importance, both bubble and spike growth are addressed. Likewise, the cases of growth during both the acceleration and deceleration phases of an implosion (i.e., on exterior as well as interior spherical interfaces) are treated. For each case (bubble- and spike-type perturbations and both acceleration and deceleration phases), the model reveals initial growth similar to the predictions of the Layzer model followed at late times by an enhancement of growth. Good agreement with two-dimensional (2D) hydrodynamic simulations is found in all cases up until the development of any secondary instabilities, notably KH roll-up. It should be noted that, at least for typical ICF conditions, once the nonlinear phase of growth has been reached, convergence by only factors of 2–3 remains for the imploding shell. By design, only linear growth occurs during the preceding factor of ~ 10 convergence. It is shown below, however, that even for the relatively modest convergence factors experienced during the nonlinear RT phase, substantial enhancements of growth over the predictions of the Layzer model can occur.

This paper is organized as follows. Section II discusses the general considerations necessary to formulate a Layzer-type model in converging geometry and the important distinction leading to either bubble-type or spike-type interface solutions is identified. In Sec. III, the formulas for the bubble amplitudes for both acceleration and deceleration phases are derived. Comparisons of the model with 2D computer simulations are made. In Sec. IV, the analogous formulas for the amplitudes of spikes in both acceleration and deceleration phases are found. Again, comparisons with 2D computer simulations are given. Section V summarizes and discusses possible directions of future work.

II. FORMULATION FOR CONVERGING GEOMETRY

For the planar case, two fundamental approximations are made in constructing Layzer-type models. The first approximation is that, at least local to the bubble apex or spike tip, the velocity field can be well represented by retaining only the lowest-order mode in the expansion of the velocity potential. In principle, an infinite number of modes should be retained to match the given initial conditions. As shown by Kull [18], however, the higher-order modes rapidly decay relative to the fundamental in the neighborhood of the bubble apex (or spike tip) such that the very useful simplification of retaining only the first mode is allowed. The second fundamental approximation of the Layzer model is that the dynamical equation for bubble or spike growth (i.e., the Bernoulli integral), which should in principle be satisfied at every point along the interface, also need only be satisfied locally to the bubble apex or spike tip in order to determine approximately the interface motion. In essence, the Layzer model is fully nonlinear in the perturbation amplitudes but local in position; i.e., it includes all orders in the perturbation amplitude but only the leading orders in position.

Given the accuracy with which the Layzer predictions match both simulations and experiment, the underlying approximations are apparently well justified and will be exploited here. However, two essential modifications are required to adapt a Layzer-type model to spherically converging interfaces. First, in the planar case, rigid, cylindrical walls are assumed to enclose the axis-symmetric bubble or spike of interest. This simplified boundary condition is an approximate representation of the bounding effect of several surrounding, comparable bubbles or spikes. For the spherical case, these cylindrical walls must be replaced with conical bounding walls in a spherical coordinate system. Here, the apex of the cone corresponds to the fixed center of the imploding sphere and its walls capture the effect of the encroachment of neighboring bubbles or spikes on the central bubble or spike over the course of the implosion.

Second, a properly spherical acceleration of the imploding interface must be considered. In the planar problem, a uniform, rectilinear acceleration of the interface is exactly equivalent to a uniform gravitational field. The effect of the acceleration of the interface may then easily be incorporated into the Bernoulli integral as an effective gravity in the frame of the interface. This equivalence, however, is no longer valid for a spherically imploding interface. Applying a uniform gravitational field to the problem of a bubble rising within a cone is the physical equivalent of setting the entire sphere into accelerated, rectilinear motion, which is not relevant to instabilities of the imploding surface. One means of

properly capturing the effect of acceleration and convergence of the interface is to consider the flow in a (primed) coordinate system moving with respect to the fixed (unprimed) coordinates according to $\{r'=r/h(t), \theta'=\theta, t'=t\}$. Here $h(t)$ is the scale factor describing the radial contraction of the primed coordinates with respect to the unprimed coordinates. In the contracting frame, the unperturbed interface corresponds to a fixed radial position, which may be taken as $r' \equiv 1$. In the fixed frame, the unperturbed interface recedes to smaller r in proportion to the decrease of $h(t)$. The character of this transformation is readily identified with that of a self-similar spherically converging flow as described by Kidder [28].

Recognizing these two modifications, the following approach is then adopted to construct a spherically convergent nonlinear RT model. Like Layzer's formulation, only the fundamental mode of the velocity potential is retained in describing the flow. Here, appropriate to the conical boundaries, Legendre functions multiplied by powers of the radius will replace Bessel functions multiplied by exponentials. Importantly, this choice of velocity potential amounts to stipulating incompressible flow of the fluid but only for the (primed) frame moving with the interface; the corresponding flow in the fixed frame will automatically prove to be properly compressible. The effect of compressibility, central in the spherical implosions of interest, is thus retained in the model but (conveniently) is separated from the RT dynamics by transforming to the contracting frame. The velocity potential ansatz is then substituted into the Bernoulli integral evaluated on the interface and the equation of motion of the fluid interface in the contracting (primed) frame. This system is then solved for the bubble or spike amplitude to leading order in the angular distance from the cone axis but retaining nonlinearities in the perturbation amplitudes.

Transforming the velocity potential, the Bernoulli integral, and the equation of motion for the fluid interface to the contracting frame leads to

$$\phi' = h^{-2}\phi + \frac{(r')^2}{2}\frac{\dot{h}}{h} + \Phi(t'), \tag{1a}$$

$$F(t') = \phi'_{t'} - \frac{|\nabla'\phi'|^2}{2} - \frac{\gamma}{\gamma-1}\frac{p'}{\rho'} + 2\frac{\dot{h}}{h}\phi' - \left.\frac{(r')^2}{2}\frac{\ddot{h}}{h}\right|_{S'=0}, \tag{1b}$$

$$0 = S'_{t'} - \nabla'\phi'\cdot\nabla' S'. \tag{1c}$$

Here ϕ is the velocity potential and $\{S'=0\}$ denotes the location of the fluid interface. Subscripts denote partial differentiation, overdots denote total derivatives with respect to time, and $\Phi(t')$ and $F(t')$ are arbitrary functions of time. The two inertial terms appearing in Eq. (1b) play the role of gravitational potentials in the interface frame but correctly incorporate the spherical nature of the flow. γ is the usual ratio of specific heats, and an ideal gas equation of state is also assumed.

Considering first the case of acceleration phase growth, the appropriate ansatz for the velocity potential in the interface frame is

$$\phi' = A'(t')(r')^{\nu}P_{\nu}(\cos\theta') \Leftrightarrow \phi = -\frac{r^2}{2}\frac{\dot{h}}{h} + A(t)r^{\nu}P_{\nu}(\cos\theta)$$

where the second line follows from Eq. (1a) and neglecting $\Phi(t')$. The automatic connection between incompressible flow in the (primed) interface frame and the appropriately compressing flow in the (unprimed) fixed frame is evident. Though ϕ' is constructed so that its Laplacian is zero, ϕ acquires from Eq. (1a) a term resulting in a nonzero Laplacian and corresponding to the appropriate radially compressing flow. Here $A'(t') \equiv h^{\nu-2}(t)A(t)$ is the time-dependent nonlinear perturbation amplitude to be determined and ν is the spherical mode number determined by the boundary condition that there be no flow through the cone walls. The arbitrary function $\Phi(t')$ can be incorporated into $F(t')$ without loss of generality. Note that, even though the Bernoulli integral is satisfied only locally near the bubble apex or spike tip, the velocity potential is chosen to satisfy boundary conditions at the cone walls—i.e., for finite values of θ. This is necessitated by the elliptic nature of Laplace's equation which, for incompressible flow, connects the flow near the apex to boundary conditions at an arbitrary distance from the apex.

Note, also, that the choice of velocity potential is well behaved at $r=0$. This is in contrast to the choices made by Plesset [13] and Yedvab *et al.* [23] in which the potential diverges as $1/r$ near $r=0$. For flows well removed from the origin or axis, the potential used by Plesset and Yedvab *et al.* may afford an adequate approximation, but in the presence of strong convergence (the case of interest) is probably no longer valid. The potential chosen here is limited in its own right by strictly describing only the implosion of a filled sphere (i.e., with a nonzero density at $r=0$) and not the finite thickness shells typical of ICF. It is, nevertheless, an acceptable approximation to capture the essential effects of convergence on acceleration phase growth. The calculation may be carried through using the velocity potential ansatz appropriate to a finite-thickness shell (i.e., including terms both growing and decaying in r). The considerable added expense in algebra, however, appears to yield little enhancement in physical content.

Since the velocity potential in the primed frame is incompressible by construction, the fluid density evolves only due to the background radially compressing component of the flow:

$$\rho = \exp\int dt\nabla^2\phi = \rho_0(\vec{r}_0)h^{-3}(t),$$

where $\rho_0(\vec{r}_0)$ is the Lagrangian value of the fluid density—i.e., density of the fluid particle at its initial location—and the integral is computed along the Lagrangian trajectory of the fluid particle. For an adiabatic implosion, the fluid pressure is given in turn by $p=p_0(\vec{r}_0)[\rho/\rho_0(\vec{r}_0)]^{\gamma}$. Since the Bernoulli integral need only be evaluated along the fluid interface, which will be assumed an isochore at $t=0$, the density

and pressure for all times may simply be taken as

$$\rho = \rho_0 h^{-3}(t) \quad \text{and} \quad p = p_0 h^{-3\gamma}(t) \text{ on } \{S=0\},$$

with ρ_0 and p_0 constants.

Characterizing the interface in the moving frame by $S = R(\theta,t) - r$ with $R(\theta,t) = a(t) + b(t)\theta^2 + O(\theta^4)$ and substituting the chosen ϕ into Eq. (1c) yields

$$0 = S_t - \nabla\phi \cdot \nabla S = \dot{a} + \nu A a^{\nu-1} + \theta^2 \left\{ \dot{b} + \nu(\nu-1)Aa^{\nu-2}b + \nu(\nu+1)Aa^{\nu-2}b - \frac{\nu^2(\nu+1)}{4}Aa^{\nu-1} \right\} + O(\theta^3). \quad (2)$$

From Eq. (2) forward, all equations are written in the contracting frame. For clarity of notation, the primes have hence been dropped, but all quantities should now be interpreted as belonging to the contracting frame. The fixed frame results can easily be obtained by inserting the appropriate factors of $h(t)$—e.g., as in Eqs. (1).

Requiring a solution at the first two orders of θ in Eq. (2) determines the perturbation amplitude $A(t)$ and the interface curvature $b(t)$ in terms of the bubble (or spike) amplitude $a(t)$:

$$A = -\frac{1}{\nu} a^{1-\nu}\dot{a} \quad \text{and} \quad b = \frac{\nu}{4}\frac{\nu+1}{2\nu-1}a + c_0 a^{2\nu}.$$

Here, c_0 is an integration constant which sets the initial curvature of the interface. The general interface shape is then

$$R(\theta,t) = a(t) + \left\{ \frac{\nu}{4}\frac{\nu+1}{2\nu-1}a(t) + c_0 a^{2\nu}(t) \right\}\theta^2 + O(\theta^4). \quad (3)$$

In typical applications, the mode numbers of interest will be in the range of $\nu = 20-200$. For such large values of ν, the general interface shape, Eq. (3), has two evident distinguished limits. For solutions for which the interface radial position $a(t)$ is a decreasing function of time, the second term of the curvature will *very rapidly* become negligible compared to the first. The interface shape may then be approximated as

$$R(\theta,t) \to a(t)\left\{ 1 + \frac{\nu}{4}\frac{\nu+1}{2\nu-1}\theta^2 \right\}, \quad \nu \gg 1. \quad (4)$$

Solutions where the radial location of the interface decreases with time during the acceleration phase represent bubbles of light fluid penetrating into the dense sphere. Equation (4) is hence taken to characterize the shape of bubbles during the acceleration phase.

By contrast, for solutions for which $a(t)$ is an increasing function of time, the first term of the curvature rapidly becomes negligible compared to the second, and the interface shape may then be approximated as

$$R(\theta,t) \to a(t) + c_0 a^{2\nu}(t)\theta^2, \quad \nu \gg 1. \quad (5)$$

Such solutions correspond to acceleration phase spike-type growth. For reasonable values of c_0—i.e., initial interface curvatures—the flow should asymptote to one of these possible shapes depending on the value of $\dot{a}(t=0)$. In Ref. [29], the initial condition $c_0 = 0$ was chosen specifically to select the bubble-type interface. Note that, like the background implosion, the bubble shape is self-similar in the sense of having a separable dependence on angle and time; i.e., it retains its curvature in θ and only scales its amplitude with the implosion. Spikes, by contrast, asymptote to infinite curvature. In the appropriate limit, both of these results can be shown to comport with the planar results of Refs. [15] and [22].

III. BUBBLE GROWTH

A. Acceleration phase

Addressing first the case of acceleration phase bubble growth, the bubble-type solution, Eq. (4), is selected for characterizing the interface $\{S=0\}$. Substituting the expressions for $A(t)$, $b(t)$, ρ, and p into the Bernoulli integral (again in the moving frame) and expanding the result to $O(\theta^2)$ leads to two coupled equations for the implosion scale factor $h(t)$ and bubble amplitude $a(t)$:

$$O(\theta^0): \quad -\frac{\nu}{2}\left(\frac{R_0}{t_c}\right)^2 h^{1-3\gamma} = a\ddot{a} + \left(1 - \frac{\nu}{2}\right)\dot{a}^2 + 2\frac{\dot{h}}{h}a\dot{a} + \frac{\nu}{2}\frac{\ddot{h}}{h}a^2,$$

$$O(\theta^2): \quad 0 = a\ddot{a} + \frac{1-2\nu}{2}\dot{a}^2 + 2\frac{\dot{h}}{h}a\dot{a} - \frac{\nu}{\nu-1}\frac{\ddot{h}}{h}a^2. \quad (6)$$

The constants R_0 and t_c are set by the initial and boundary conditions in pressure and density and determine the length and time scales of the implosion.

In principle, the $O(\theta^2)$ equation should be solved for $a(t)$ as a functional of $h(t)$ and the result substituted into the $O(\theta^0)$ equation to find a single self-consistent solution for $h(t)$. Such an exact solution to Eqs. (6) could not be found. Equations (6) may, of course, easily be integrated numerically. To find an approximate analytical solution, however, the change of variables $w(t) \doteq h(t)a^{3/2-\nu}(t)$ can be used to reduce the $O(\theta^2)$ equation to Schrödinger form

$$0 = \ddot{w} + \Lambda^2(\nu)\frac{\ddot{h}}{h}w, \quad \Lambda(\nu) \doteq \sqrt{\frac{\nu(3-2\nu)}{2(1-\nu)} - 1}. \quad (7)$$

For a sufficiently slowly evolving "potential" $\Lambda^2(\nu)\ddot{h}/h$, the approximate bubble amplitude may then be calculated by the WKB method:

$$a(t) \sim \left\{ \frac{1}{h}\exp\left[\pm\Lambda(\nu)\int_0^t dt\sqrt{-\ddot{h}/h} \right] \right\}^{1/(3/2-\nu)}. \quad (8)$$

This expression for $a(t)$ could be substituted into the $O(\theta^0)$ equation and an iterative approximation for $h(t)$ developed. A more tractable approach, however, is to note that, in the limit of large ν, the $O(\theta^0)$ equation reduces to Kidder's equation for the scale factor of an unperturbed self-similar implosion [28]:

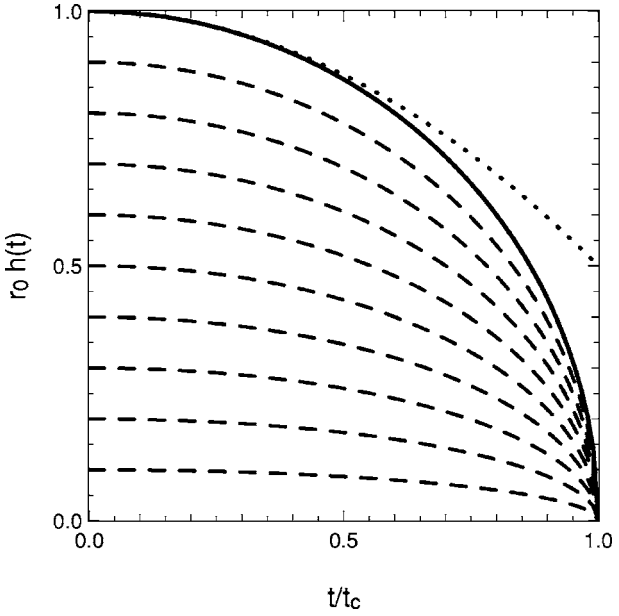

FIG. 1. Implosion diagram of an accelerating, Kidder-type implosion. The interface trajectory is shown as the solid line and sample fluid particle trajectories as the dashed lines. For comparison, the trajectory of a constant acceleration or "free-falling" implosion is shown by the dotted line.

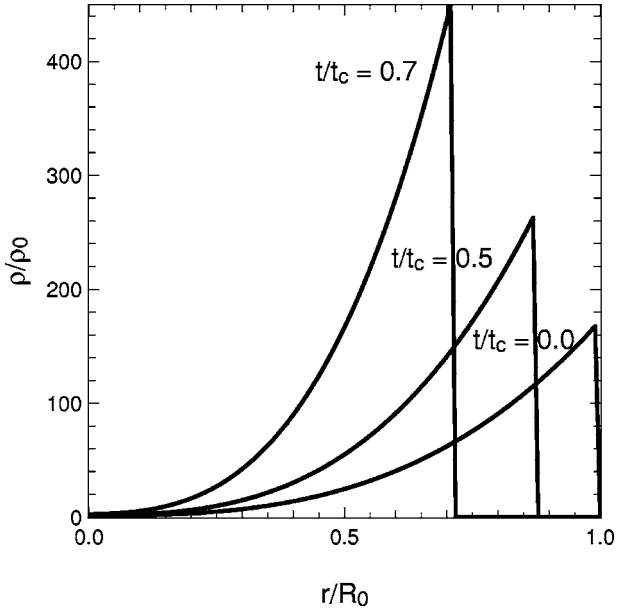

FIG. 2. Sequence of radial density profiles corresponding to an accelerating, Kidder-type implosion. The density scale has been normalized by the density at $r=0$ and $t=0$.

$$h^{3\gamma-2}\ddot{h} \simeq \text{const} \equiv -\frac{1}{t_c^2}, \quad \nu \gg 1. \tag{9}$$

For the case of $\nu \gg 1$, it is then acceptable to approximate $h \simeq h_{\text{Kidder}}$. Indeed, this limit might have been expected from the form chosen for the transformation to the contracting frame.

Specializing to $\gamma=5/3$, the self-similar Kidder scale factor is $h(t)=\sqrt{1-(t/t_c)^2}$. A Lagrange diagram of this self-similar implosion is shown in Fig. 1 where the heavy dark line denotes the nominal edge of the imploding sphere and the dashed lines the trajectories of individual fluid elements. For comparison, the trajectory of a constant acceleration or "free-falling" implosion (i.e., $g=$const) is shown with the dotted line. The self-similar implosion collapses to zero volume at $t=t_c$ and hence experiences substantially greater acceleration late in the implosion than the free fall case. A sequence of the corresponding density profiles (dictated by the assumption of self-similarity) is shown in Fig. 2 where the density scale has been normalized to the density at $r=0$ and $t=0$. Despite the very strong constraint of self-similarity, such shell-type, self-similar profiles reasonably approximate the radial profiles expected for realistic ICF implosions.

Finally, substituting the Kidder formula for $h(t)$ into the WKB solution Eq. (8) results (still for $\gamma=5/3$) in a simple formula for the bubble amplitude as a function of time:

$$a(t) \sim \left\{ \frac{1}{h}\left[\left(\frac{1+t/t_c}{1-t/t_c}\right)^{\sqrt{\nu}/2} + \left(\frac{1+t/t_c}{1-t/t_c}\right)^{-\sqrt{\nu}/2} \right] \right\}^{1/(3/2-\nu)}, \quad \nu \gg 1. \tag{10}$$

Here, the combination of exponentially growing and decaying solutions from Eq. (8) has been chosen to satisfy the initial conditions $a(t=0)=1$ and $\dot{a}(t=0)=0$. It is also possible to choose a combination such that the initial bubble velocity matches the corresponding Layzer velocity of the planar problem $\dot{a}(t=0)=-1/\sqrt{\nu}$, such as in [29].

Equation (10) was verified by comparing with 2D arbitrary Lagrangian-Eulerian (ALE) hydrodynamics simulations run with the HYDRA code [30]. For a given mode number ν, a simulation was initialized with slip boundary conditions on the cone walls and a Kidder-type pressure source applied through a low-density pusher material (approximating $\mathcal{A}=1$) to the fluid interface. The radial density profile within the dense fluid was initialized as prescribed by Kidder [28], and the interface was nonlinearly perturbed in accordance with the initial second-order bubble shape, Eq. (4). The simulation was run with azimuthal symmetry about the cone axis, and 25 zones were used to resolve the half-angle of the cone. Depending on the mode number, the number of radial zones was chosen to keep individual zones approximately square in aspect ratio. Considerable ALE relaxation of the mesh was required throughout the simulation.

An example sequence of snapshots of bubble growth from a simulation with $\nu=80$ is shown in Fig. 3. The dense fluid is shown in red, and the low-density pusher appears in blue. Mixing of the fluids due to the ALE relaxation of the mesh results in the yellow-colored boundary zones. The broad bubble is seen to advance down the axis of the cone, while the conical spike sheets run up the cone walls. By $t/t_c=0.75$, KH roll-up of the the spike tips can be seen, though this does not appear to affect the bubble growth substantially.

Figure 4 illustrates the bubble height as measured from the simulation in Fig. 3 (shown as the solid line) in comparison with the WKB solution from Eq. (10) (shown as the dotted line) and the Layzer prediction (shown as the dashed line). Also shown are the analogous simulation and WKB

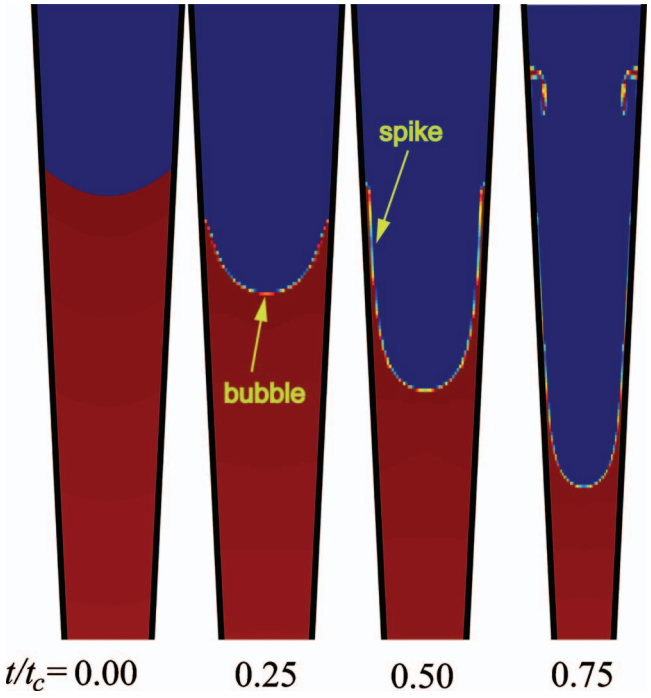

FIG. 3. (Color) Snapshots of bubble growth from a HYDRA simulation of RT growth during the acceleration phase with $\nu=80$. Red denotes the dense fluid and blue the low-density pusher. To illustrate the bubble evolution, each snapshot is centered approximately about the location of the bubble apex at the corresponding time.

results for modes $\nu=20$ and 40. In each case, following a brief acceleration period, there is a period of linear growth with time at approximately the Layzer velocity. Later in the implosion, however, the HYDRA and WKB results all demonstrate substantially faster bubble growth than predicted by the Layzer model. Good agreement between the simulation results and the theoretical expectations is seen throughout the implosion. The results of numerically integrating Eqs. (6) (not shown for clarity) were also in excellent agreement with the WKB solution for all mode numbers. The dashed curve representing the Layzer prediction includes the effects of the time-varying acceleration and wavelength of the bubble over the course of the implosion. Comparing this curve with the WKB and simulation results indicates that the enhanced growth in the latter two cases is not merely the result of enhanced acceleration or a time-dependent wavelength but a unique effect of the spherical convergence.

B. Deceleration phase

Once the case of acceleration phase bubble growth has been analyzed, the deceleration phase follows directly. By reversing the sign of the constant in Eq. (9), the solution of Kidder's equation can describe a self-similar spherically stagnating flow [31]. Physically, this corresponds simply to reversing the direction of the pressure gradient from radially accelerating to decelerating. Again, for $\gamma=5/3$ and for a given initial implosion velocity $\dot{h}(t=0)=c$, the implosion scale factor is now given by $h(t)=\sqrt{1+ct_c-ct_c(t/t_c-1)^2}$.

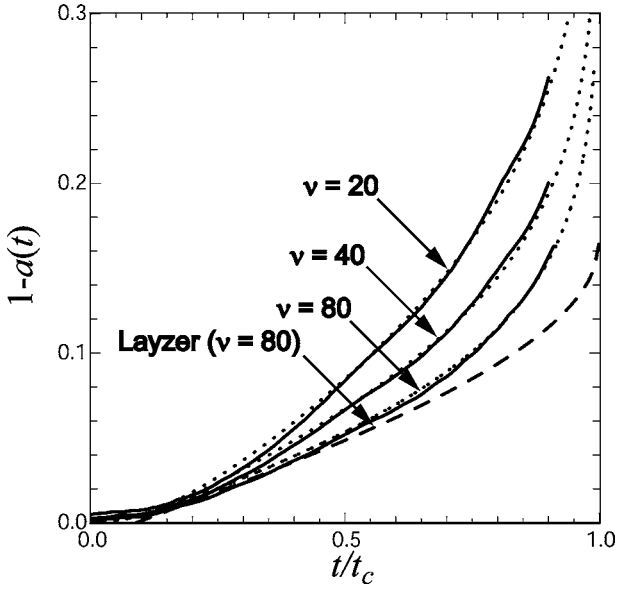

FIG. 4. Comparison of normalized bubble heights in the frame moving with the interface from the HYDRA simulation of Fig. 3 (solid line), the WKB solution of Eq. (10) (dotted line), and the Layzer prediction (dashed line). Results for modes $\nu=20$ and 40 are also shown. Here and below the length scale has been normalized to the initial shell radius—i.e., $R_0\equiv 1$.

A Lagrange diagram of such a self-similar stagnation is shown in Fig. 5 for $c=-0.9$. The heavy dark line again denotes the putative inner edge of the imploding shell and the dotted line an interface undergoing constant deceleration at the peak deceleration experienced in the self-similar case.

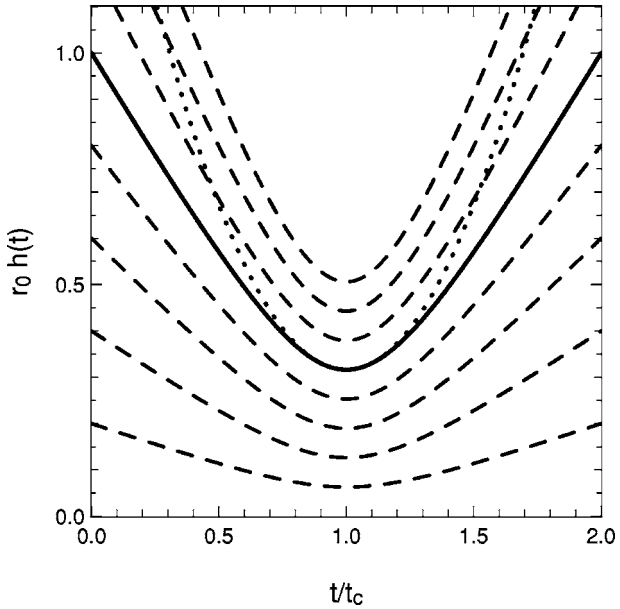

FIG. 5. Implosion diagram of a decelerating, Kidder-type implosion with initial implosion velocity of $c=-0.9$. The interface trajectory is shown as the solid line and sample fluid particle trajectories as the dashed lines. For comparison, the dotted line shows the trajectory of a "free-falling" implosion decelerating at the peak deceleration of the self-similar case.

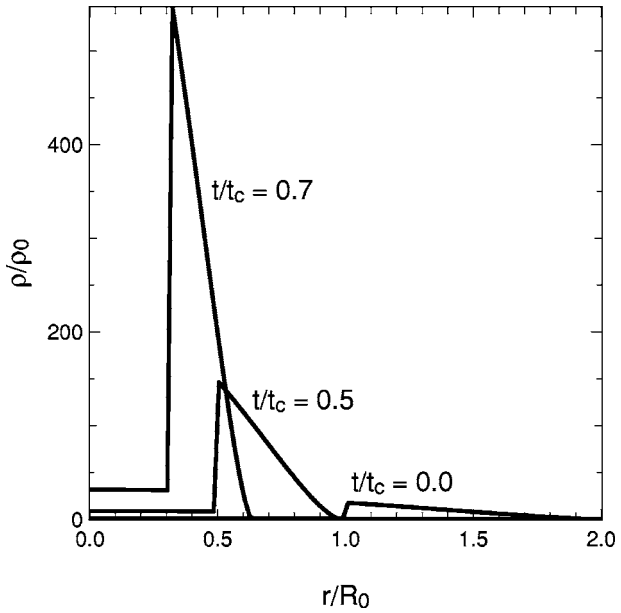

FIG. 6. Sequence of radial density profiles corresponding to a decelerating, Kidder-type implosion. The density scale has been normalized by the density at $r=0$ and $t=0$. An initial aspect ratio of $R_{\text{out}}/R_0=2.0$ at $t=0$ has been chosen, which corresponds to an Atwood number at the shell-gas interface of $\mathcal{A}=0.90$.

Individual fluid particles (dashed lines) are seen to follow hyperbolic trajectories and reach peak compression at $t=t_c$.

A sequence of the corresponding density profiles is shown in Fig. 6 with the density scale normalized by the density at $r=0$ and $t=0$. Again, the self-similar profiles give a quite plausible approximation of the profile of a dense shell collapsing on a low-density, high-pressure hot spot, as in realistic ICF implosions. Unlike the acceleration phase self-similar profiles, here the Atwood number cannot be specified independent of the shell radius. It can, however, be made sufficiently close to unity not to alter grossly the bubble evolution. In this case, a shell aspect ratio of $R_{\text{out}}/R_0=2.0$ at $t=0$ has been chosen, which corresponds to an Atwood number at the shell-gas interface of $\mathcal{A}=0.90$. Note that the self-similarity of the flow guarantees that the Atwood number is constant in time.

Turning to the description of the RT growth, the appropriate ansatz for the velocity potential in the deceleration phase is $\phi \simeq A(t) r^{-\nu-1} P_\nu(\cos\theta)$. Analogous to the acceleration phase, this choice of velocity potential is strictly valid only for the problem of a collapsing cavity immersed in an infinitely extended fluid. For the case of perturbation wavelengths short compared to the thickness of the shell, however, this choice will again prove an adequate approximation.

Mathematically, the choice of velocity potential for the deceleration case may be obtained from its acceleration phase counterpart simply by the transformation $\nu \to -\nu-1$. With this transformed mode number, the analysis of the deceleration phase then simply recapitulates the acceleration phase calculation up until Eqs. (6). In this system, the sign on the left-hand side of the $O(\theta^0)$ equation must also be reversed to correspond to the deceleration phase pressure gradient which is oppositely directed to the acceleration phase gradient. Again, in the limit of $\nu \gg 1$, this equation then reduces directly to the needed Kidder's equation for the deceleration phase scale factor $h(t)$.

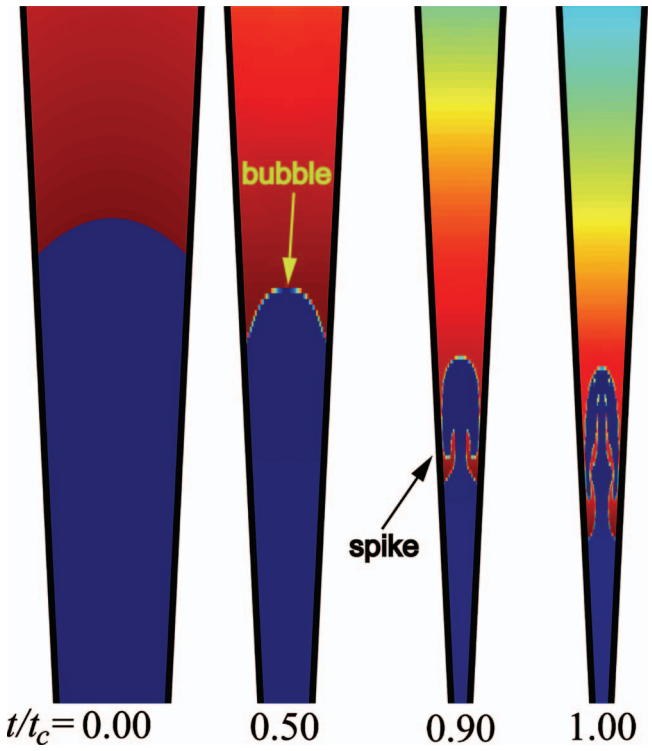

FIG. 7. (Color) Snapshots of bubble growth from a HYDRA simulation of RT growth during the deceleration phase with $\nu=80$. Each snapshot is centered approximately about the location of the bubble apex at the corresponding time. The color scale gives the fluid density with red the dense shell and blue the low-density gas.

With $h(t)$ determined, the solution for the bubble amplitude $a(t)$ then follows as before from the WKB solution of Eq. (8). After transforming the mode number to its negative, however, $\Lambda(\nu)$, as defined in Eq. (7), is a purely imaginary quantity. The WKB result, hence, corresponds to the expected stable oscillations unless $\ddot{h}(t)$ also reverses sign. This is, of course, precisely the case for the stagnating shell. Hence, substituting the stagnation $h(t)$ (for $\gamma=5/3$) into the WKB expression with $\nu \to -\nu-1$ gives the expected growing bubble amplitude

$$a(t) \sim h^{2/(2\nu+5)} \exp\left\{ \frac{1}{\sqrt{\nu}} \left[\tan^{-1}\left(\sqrt{\frac{-c}{1+c}} (t/t_c - 1) \right) - \tan^{-1}\left(-\sqrt{\frac{-c}{1+c}} \right) \right] \right\}, \quad \nu \gg 1. \tag{11}$$

Again, Eq. (11) was compared with 2D HYDRA simulations. As shown in Fig. 7, the radial density profile was initialized as determined by the self-similarity and shown in Fig. 6. Likewise, the nonlinear perturbation applied to the interface reverses its curvature relative to the acceleration phase in accordance with the sign change of ν in Eq. (4). For the deceleration phase, the shell is initialized with the implosion velocity c, and no external driving pressure need be

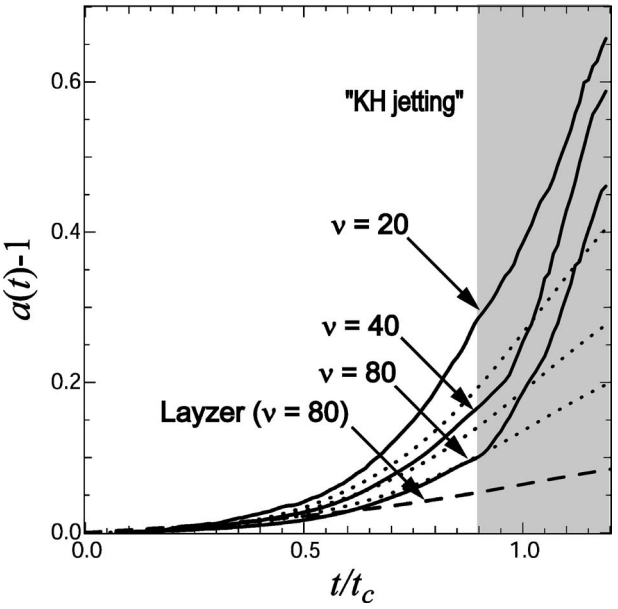

FIG. 8. Comparison of normalized bubble heights in the frame moving with the interface from the HYDRA simulation of Fig. 7 (solid line), the WKB solution of Eq. (10) (dotted line), and the Layzer prediction (dashed line). The shaded region marks the onset of KH vortex generation, jet formation by vortex interference, and subsequent bubble acceleration. Results for modes $\nu=20$ and 40 are also shown.

applied. ALE relaxation of the mesh identical to the acceleration case was also used.

Analogous to Fig. 4, Fig. 8 shows a plot of the measured bubble height from the simulation compared to the WKB results, Eq. (11), and to the Layzer prediction. The time-dependent wavelength and deceleration are again included in computing the Layzer curve. The agreement appears quite close between the WKB and simulation results up until $t/t_c \simeq 0.90$. Again, both indicate substantially greater bubble growth than expected from the Layzer prediction. Also as before, the result (not shown) of numerically integrating the coupled equations, Eq. (6), for the deceleration phase was in very close agreement with the WKB result.

After $t/t_c \simeq 0.90$, the measured bubble height diverges strongly from the Eq. (11) prediction. Inspecting the snapshots in Fig. 7 shows that noticeable KH roll-up has occurred by this time. In the final frame, at $t/t_c \simeq 1.00$, the vortices formed at the spike tips have begun to mutually interfere due to the confining effect of the cone walls, itself a model of the effect of convergence. As evident in a plot of the fluid velocity field, this vortex interference causes a high velocity jet of fluid to form along the cone axis. The impact of this jet with the bubble apex likely accounts for the sudden enhancement of the bubble growth. These complicated secondary effects are clearly not included in the Layzer-type model presented here. Nevertheless, Eq. (11) affords a good approximation of the bubble growth up until the time of peak compression.

Also shown in the figure are the equivalent results for modes $\nu=20$ and 40. For mode $\nu=40$, the agreement between the WKB and simulation results is again fairly close until $t/t_c \simeq 0.95$. At this time, the interference of KH vortices again leads to jet formation and invalidates the predictions of the Layzer-type model. The bubble height in the $\nu=20$ case grows notably faster in the simulation than for the WKB result, even before the development of secondary KH instabilities. Taken together, the curves for $\nu=40$ and 20 suggest a trend of successively greater divergence of the WKB predictions from the simulation results with decreasing mode number. This trend is conceivably due to the very pronounced, and ultimately nonlocal, convergence effects experienced by such long-wavelength modes in the very confined geometry of the late stagnation phase. Effectively, the interference between spikes, which leads to the sudden divergence in the $\nu=80$ curve, sets in earlier in the increasingly limited space available at lower mode numbers $\nu=40$ and 20. The validity of Eq. (11) only for the limit $\nu \gg 1$ is indeed evident.

IV. SPIKE GROWTH

Turning now to the case of spike growth, the spike-type solution of the interface equation (5) must be selected for the interface $\{S=0\}$. The procedure of calculating the spike amplitude as a function of time is otherwise equivalent to the bubble case.

A. Acceleration phase

With $b(t)=c_0 a^{2\nu}(t)$ and $\phi=A(t)r^\nu P_\nu(\cos\theta)$ for the acceleration phase, the Bernoulli integral on the interface expands at the first two orders in θ as

$$O(\theta^0): \quad -\frac{\nu}{2}\left(\frac{R_0}{t_c}\right)^2 h^{1-3\gamma} = a\ddot{a} + \left(1-\frac{\nu}{2}\right)\dot{a}^2 + 2\frac{\dot{h}}{h}a\dot{a} + \frac{\nu}{2}\frac{\ddot{h}}{h}a^2,$$

$$O(\theta^2): \quad 0 = \left[\frac{b}{a} - \frac{\nu+1}{4}\right]\left[a\ddot{a} + (1-\nu)\dot{a}^2 + 2\frac{\dot{h}}{h}a\dot{a}\right] - \left[\frac{\nu^2-1}{4} + 2(1-\nu)\frac{b}{a}\right]\frac{\dot{a}^2}{2} + \frac{b}{a}\frac{\ddot{h}}{h}a^2. \qquad (12)$$

As should be expected, the first equation—i.e., the purely radial dynamics of the implosion—is unchanged, and its solution can again be approximated as a self-similar Kidder-type implosion for $\nu \gg 1$. As written, the $O(\theta^2)$ equation is no longer of Schrödinger type and a WKB approximation can no longer be used. However, since $b/a \to \infty$ extremely rapidly for a spike, a substantial simplification is possible by keeping only the leading terms in b/a. Retaining only these terms leads to the much simpler $O(\theta^2)$ equation

$$0 \simeq a\ddot{a} + 2\frac{\dot{h}}{h}a\dot{a} + \frac{\ddot{h}}{h}a^2 = \frac{a}{h}\frac{d^2}{dt^2}(ah). \qquad (13)$$

This equation may be integrated directly to yield

$$a(t) = \frac{[\dot{a}(0) + a(0)\dot{h}(0)]t + a(0)}{h(t)}. \qquad (14)$$

Notably, the mode number dependence has been lost in this solution. This is again as should be expected given that

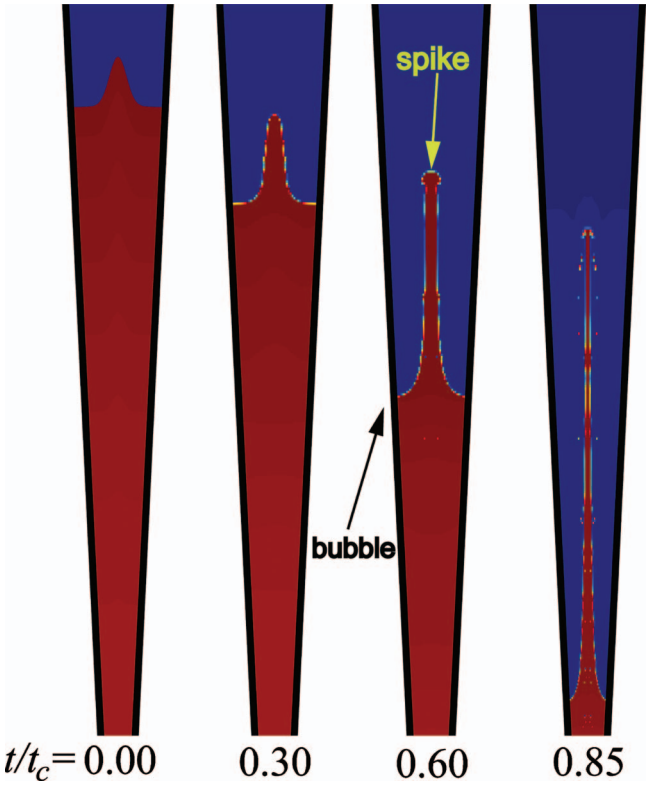

FIG. 9. (Color) Snapshots of spike growth from a HYDRA simulation analogous to Fig. 3. The simulation is run identically to Fig. 3 but with a spike-type initial interface shape instead of a bubble-type shape.

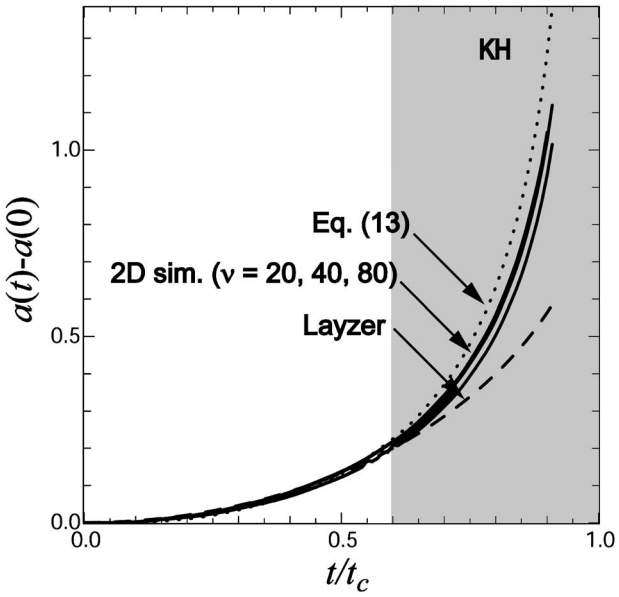

FIG. 10. Comparison of spike heights in the frame moving with the interface from the HYDRA simulation of Fig. 9 (solid line), the solution given by Eq. (14) (dotted line), and the Layzer prediction (dashed line). The shaded region marks the onset of KH vortex growth. Results for modes $\nu=20$ and 40 are also shown.

the spike represents a narrow projection of fluid running down the cone axis and so is increasingly disconnected from the bounding walls. Indeed, in agreement with the planar results of Zhang [22], the interface curvature at the spike tip asymptotes to infinity ($b/a\rightarrow\infty, t\rightarrow\infty$) in the approximation which lead to Eq. (13).

Moreover, it should be noted that Eq. (14) describes the spike amplitude in the interface (contracting) frame. In the fixed frame, obtained simply by multiplying $a(t)$ in the interface frame by the scale factor $h(t)$, Eq. (14) describes a spike continuing in free streaming motion at its initial velocity $\dot{a}(t=0)$, while the interface is effectively accelerating away from the spike tip. [Equation (13) is, in fact, the equation for unaccelerated motion of the spike tip in the fixed frame.] This is likewise the direct analogue of the result where the freely falling spike tip in the frame of a planar interface corresponds to fluid at rest in the fixed frame.

Figure 9 shows the simulated growth of a RT spike during the acceleration phase. The input parameters for this simulation are identical to those of Fig. 3 except that the bubble-type initial perturbation has been replaced by a Gaussian spike-type initial perturbation. The spike is seen to lengthen along the axis of the cone while the surrounding bubbles now run down the cone walls. KH broadening of the spike tip evidently prevents the tip from asymptoting toward the infinite curvature predicted from the Layzer-type solution. This is an inevitable byproduct of the finite density ratio allowable in the simulation. Nevertheless, good agreement between the predicted and measured spike amplitudes is seen in Fig. 10.

The gradual divergence of the predicted and measured amplitudes at late times is likely due to the KH growth. The planar Layzer result (including the time-dependent acceleration) again substantially underpredicts the spike amplitude. Doubling the resolution did not alter the measured spike amplitude despite adding much more refinement to the KH vortices. Also shown in the figure are the simulation results for modes $\nu=20$ and 40. That the results are virtually identical for the range $\nu=20-80$ validates that spike growth is indeed asymptotically independent of mode number, as predicted by Eq. (14). Simulations with a range of initial spike amplitudes and spike widths were also found to agree well with Eq. (14).

B. Deceleration phase

As was seen in the case of bubble growth, the acceleration phase results may be transformed into deceleration phase results simply by transforming $\nu\rightarrow-\nu-1$ and using the appropriate deceleration phase $h(t)$. This transformation likewise applies to the case of spike growth. Furthermore, since the solution of Eq. (13) is independent of the mode number in the limit $\nu\gg1$, Eq. (14) and its implications evidently apply to the deceleration phase as much as to the acceleration phase.

Figure 11 shows the growth of a spike in a simulation analogous to Fig. 7 but with $c=-0.95$, $\mathcal{A}=0.95$, and a spike-type initial interface shape. The higher Atwood number in this simulation (accompanying the choice of a lower aspect ratio shell) delays the onset of KH instability as compared to Fig. 7. The measured spike height is shown in Fig. 12, again in good agreement with the prediction of Eq. (14) for t/t_c

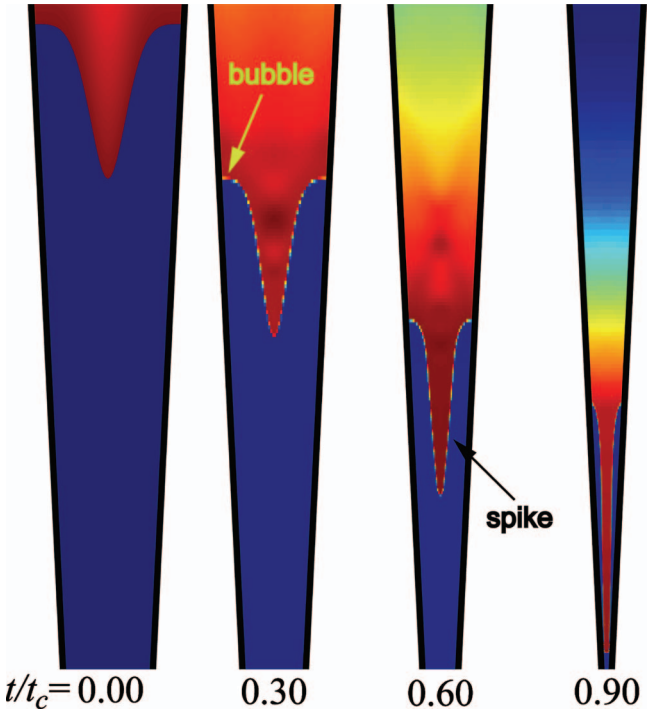

FIG. 11. (Color) Snapshots of spike growth from a HYDRA simulation analogous to Fig. 7 but with $c=-0.95$, $\mathcal{A}=0.95$, and a spike-type initial interface shape. Each snapshot is centered approximately about the location of the spike tip at the corresponding time.

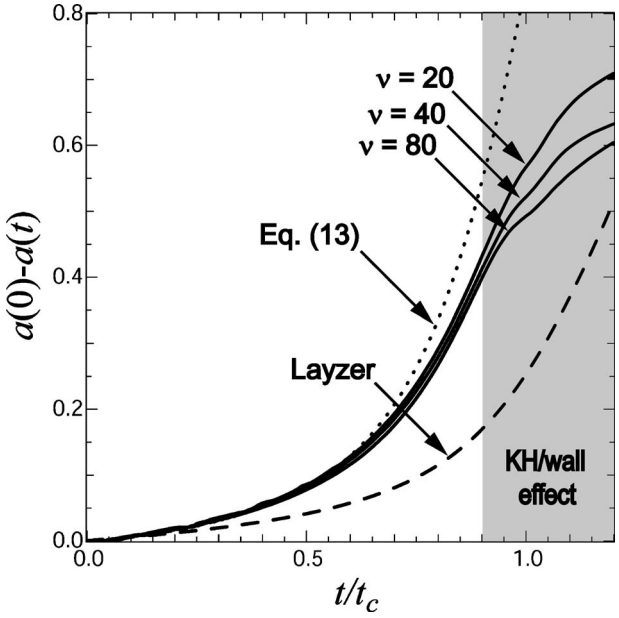

FIG. 12. Comparison of spike heights in the frame moving with the interface from the HYDRA simulation of Fig. 11 (solid line), the solution of Eq. (13) (dotted line), and the Layzer prediction (dashed line). The shaded region marks the onset of KH vortex growth and collision with the cone walls. Results for modes $\nu=20$ and 40 are also shown.

<0.9 but very different from the Layzer result.

Beyond comparison with the planar Layzer result, Fig. 12 also demonstrates the dramatic impact of convergence on the saturation of deceleration phase spike growth. At $t/t_c=0.9$, Fig. 12 indicates a sudden suppression of growth as compared to Eq. (14). From Fig. 11, this evidently results from collision of the finite width spike tip with the ever-encroaching cone walls. The finite width of the spike is itself a result of KH instability of the tip, an effect not included in the model. Of course, in a physical, spherical implosion, collision with the cone walls corresponds to saturation by collision with neighboring spikes. Until this collision time, however, Eq. (14) appears to give an adequate prediction of the spike amplitude. As in Fig. 10, the results for modes $\nu=20$ and 40 are also shown and, until saturation, appear nearly indistinguishable from the result for $\nu=80$. Note that the effectively narrower cone opening, as experienced by the KH-broadened spike, evidently leads to earlier saturation with larger ν.

V. CONCLUSIONS

In summary, the Layzer model for nonlinear RT growth has been generalized to the case of spherically imploding interfaces for both the acceleration and deceleration phases of growth. Both bubble- and spike-type growth have been considered. Good agreement was found when comparing the model results with 2D numerical simulations, except in the case of stagnation phase bubble growth at low mode numbers. Divergence of the simulation results from the theoretical predictions generally appeared to be the result of the growth of secondary KH instabilities not included in the model. In all cases, growth rates initially similar to the planar Layzer predictions were obtained followed by substantial divergences between the spherical results and the planar predictions at late times.

A number of other generalizations could be imagined for the results derived here. Foremost, in all four of the cases considered, the implosion history $h(t)$ could not be programed arbitrarily but was determined self-consistently with the bubble or spike amplitude $a(t)$ through a pair of coupled differential equations, Eqs. (6) or (12). This is a fundamental property of calculating instability growth in the frame contracting according to the scale transformation chosen in Sec. II. It has been shown that, in the limit of large mode numbers, this constraint reduces to a self-similar implosion of the type introduced by Kidder. While Kidder-type self-similar implosions provide a quite reasonable approximation of ICF target behavior for both acceleration and deceleration, relaxing this constraint and allowing more generalized acceleration histories in the RT calculation would be useful. Indeed, typical ICF implosions are actually better characterized by constant, rather than self-similar, accelerations.

A second deficiency of the analysis so far is that the connection to the (linear) initial conditions remains obscure. Elucidating the connection from the linear regime results of Bell-Plesset to the nonlinear results presented here would hence be another useful generalization. This connection would presumably entail retaining the complete interface shape, as in Eq. (3) with both the bubble-type and spike-type curvature terms, in order to capture the linear amplitude curvature. The amplitude and scale factor equations which

would result from this interface shape can be expected to be much more complicated than the limiting forms for pure bubbles or spikes which appear in Eqs. (6) or (12). In principle, such complicated equations could always be solved numerically. Obtaining the correct limiting forms analytically, however, for growth in both the linear and nonlinear regimes, could give valuable insight into the character of the linear-nonlinear growth transition.

The case of instability growth in cylindrical geometry could also be addressed straightforwardly by the approach outlined here. Beyond general interest, instability growth at cylindrical interfaces would have immediate applications to z-pinch stability, as well as being a geometry in which direct comparison with experiment would be much simplified [32,33]. Likewise, ablation is known to influence substantially the growth in the linear [34] as well as nonlinear regimes [35,36]. Accounting for ablation in the spherical context would then also be useful. As a final development, incorporating the spherically accurate results derived here into a generalized Haan saturation model [37] would be very useful for ICF target design purposes. These are all subjects of current research.

ACKNOWLEDGMENTS

The authors acknowledge valuable discussions with K. O. Mikaelian and M. M. Marinak. This work was performed under the auspices of the U.S. Department of Energy by the University of California, Lawrence Livermore National Laboratory under Contract No. W-7405-Eng-48.

[1] Lord Rayleigh, *Scientific Papers* (Cambridge University Press, Cambridge, England, 1900).
[2] G. I. Taylor, Proc. R. Soc. London, Ser. A **201**, 192 (1950).
[3] J. D. Lindl, *Inertial Confinement Fusion: The Quest for Ignition and Energy Gain Using Indirect Drive* (American Institute of Physics, Woodbury, NY, 1998).
[4] D. Arnett, Astrophys. J., Suppl. Ser. **127**, 213 (2000).
[5] I. Hachisu, T. Matsuda, K. Nomoto, and T. Shigeyama, Astrophys. J. Lett. **368**, L27 (1991).
[6] T. Ebisuzaki, T. Shigeyama, and K. Nomoto, Astrophys. J. Lett. **344**, L65 (1989).
[7] L. Smarr, J. R. Wilson, R. T. Barton, and R. L. Bowers, Astrophys. J. **246**, 515 (1981).
[8] J. Arons and S. M. Lea, Astrophys. J. **207**, 914 (1976).
[9] E. A. Frieman, Astrophys. J. **120**, 18 (1954).
[10] D. H. Sharp, Physica D **12**, 3 (1984).
[11] H. J. Kull, Phys. Rep. **206**, 197 (1991).
[12] G. I. Bell, Los Alamos National Laboratory, Report LA-1321(1951).
[13] M. S. Plesset, J. Appl. Phys. **25**, 96 (1954).
[14] R. M. Davies and G. I. Taylor, Proc. R. Soc. London, Ser. A **200**, 375 (1950).
[15] D. Layzer, Astrophys. J. **122**, 1 (1955).
[16] K. I. Read, Physica D **12**, 45 (1984).
[17] H. J. Kull, Phys. Rev. A **33**, 1957 (1986).
[18] H. J. Kull, Phys. Rev. Lett. **51**, 1434 (1983).
[19] J. Hecht, U. Alon, and D. Shvarts, Phys. Fluids **6**, 4019 (1994).
[20] R. D. Richtmyer, Commun. Pure Appl. Math. **13**, 297 (1960).
[21] V. Andronov, S. M. Bakhrakh, E. E. Meshkov, V. N. Mokhov, V. V. Nikiforov, A. V. Pevnitskii, and A. I. Tolshmyakov, Sov. Phys. JETP **44**, 424 (1976).
[22] Q. Zhang, Phys. Rev. Lett. **81**, 3391 (1998).
[23] Y. Yedvab, U. Alon, D. Oron, and D. Shvarts in, Proceedings of the Sixth International Workshop Phys. Comp. Turbulent Mixing, Marseille, France, 1997, p. 528.
[24] M. J. de C. Henshaw, G. J. Pert, and D. L. Youngs, Plasma Phys. Controlled Fusion **29**, 405 (1987).
[25] H. Sakagami and K. Nishihara, Phys. Rev. Lett. **65**, 432 (1990).
[26] R. P. J. Town and A. R. Bell, Phys. Rev. Lett. **67**, 1863 (1991).
[27] T R. Dittrich, B. A. Hammel, C. J. Keane, R. McEachern, R. E. Turner, S. W. Haan, and L. J. Suter, Phys. Rev. Lett. **73**, 2324 (1994).
[28] R. E. Kidder, Nucl. Fusion **14**, 53 (1974).
[29] D. S. Clark and M. Tabak, Phys. Rev. E **71**, 055302(R) (2005).
[30] M. M. Marinak, G. D. Kerbel, N. A. Gentile, O. Jones, D. Munro, S. Pollaine, T. R. Dittrich, and S. W. Haan, Phys. Plasmas **8**, 2275 (2001).
[31] S. Atzeni and J. Meyer-ter-Vehn, *The Physics of Inertial Fusion* (Oxford Science, New York, 2004).
[32] W. W. Hsing and N. M. Hoffman, Phys. Rev. Lett. **78**, 3876 (1997).
[33] W. W. Hsing *et al.*, Phys. Plasmas **4**, 1832 (1997).
[34] S. E. Bodner, Phys. Rev. Lett. **33**, 761 (1974).
[35] D. Oron, U. Alon, and D. Shvarts, Phys. Plasmas **5**, 1467 (1998).
[36] J. Santz, J. Ramìrez, R. Ramis, R. Betti, and R. P. J. Town, Phys. Rev. Lett. **89**, 195002 (2002).
[37] S. W. Haan, Phys. Rev. A **39**, 5812 (1989).